


Article

# Parametrically Amplified Low-Power MEMS Capacitive Humidity Sensor

Rugved Likhite , Aishwaryadev Banerjee, Apratim Majumder, Mohit Karkhanis, Hanseup Kim and Carlos H. Mastrangelo \*

Department of Electrical and Computer Engineering, University of Utah, Salt Lake City, UT 84112, USA; rugved.likhite@utah.edu (R.L.); aishwaryadev.banerjee@utah.edu (A.B.); apratim.majumder@utah.edu (A.M.); mohit.karkhanis@utah.edu (M.K.); hanseup@ece.utah.edu (H.K.)

\* Correspondence: carlos.mastrangelo@utah.edu; Tel.: +1-603-714-5099

Received: 30 July 2019; Accepted: 11 September 2019; Published: 13 September 2019



**Abstract:** We present the design, fabrication, and response of a polymer-based Laterally Amplified Chemo-Mechanical (LACM) humidity sensor based on mechanical leveraging and parametric amplification. The device consists of a sense cantilever asymmetrically patterned with a polymer and flanked by two stationary electrodes on the sides. When exposed to a humidity change, the polymer swells after absorbing the analyte and causes the central cantilever to bend laterally towards one side, causing a change in the measured capacitance. The device features an intrinsic gain due to parametric amplification resulting in an enhanced signal-to-noise ratio (SNR). Eleven-fold magnification in sensor response was observed via voltage biasing of the side electrodes without the use of conventional electronic amplifiers. The sensor showed a repeatable and recoverable capacitance change of 11% when exposed to a change in relative humidity from 25–85%. The dynamic characterization of the device also revealed a response time of ~1 s and demonstrated a competitive response with respect to a commercially available reference chip.

**Keywords:** humidity sensor; low-power sensors; MEMS; parametric amplification; spring softening

## 1. Introduction

In recent decades, miniaturized humidity sensors have been realized using various transduction methods [1–7] for a wide range of applications such as improving indoor comfort in homes and automobiles, humidity monitoring in semiconductor processing facilities [8], food processing industries [9], medical facilities [10] and, Internet-of-Things (IoT) based frameworks [11]. The push for the need for low-power chemical sensors [12–14] has been quite strong due to the growing importance of IoT sensor nodes across the world.

The most commonly used humidity sensor for the applications mentioned above is the capacitive sensor, which is used in nearly 75% of the cases [3] as nearly zero DC current flows through them making them extremely low power consuming devices. These devices measure the change in capacitance caused by variations in dielectric properties or thickness of a sensing layer sandwiched between two parallel plates [15,16] when exposed to humidity. Sensors based on measuring the deflection of a microcantilever coated with a sensing polymer have also been demonstrated [17,18]. These sensors show a linear behavior, are easy to batch fabricate, and most importantly, consume nearly zero DC power. However, their Signal-to-Noise Ratio (SNR) is usually limited by electronic noise as their sense capacitance can be small in comparison to the surrounding parasitics due to their small size [19]. Amplifiers are typically used in conjunction with such sensors to obtain a stable output, which further adds to the total noise of the system and limits the SNR.

The sensitivity of capacitive hygrometers can be significantly improved if these devices have an intrinsic gain, thus reducing the dependence on noisy electronic amplifiers. This can be achieved with mechanical leveraging and parametric amplification. An example of a mechanically leveraged structure is a microcantilever device coated on one side with a sensing layer. Highly sensitive microcantilever-based sensors have been reported previously for detecting gases [18,20,21], DNA hybridization [22,23], and toxic chemical warfare agents [24]. In these devices, the exposure of the sensing film to an analyte or temperature change generates surface stress that induces bending of the free-standing cantilever either due to a reduction in interfacial surface energy or swelling of the sensing layer. High signal to noise ratio can be realized in such devices using parametric amplification while maintaining small transducer size and low power consumption by exploiting the voltage induced lateral instability in Micro-Electro-Mechanical Systems (MEMS) devices to magnify their displacement to capacitance sensitivity. This technique has been previously reported to improve the performance of a MEMS magnetometer [19], gyroscope [25], hair-flow sensor [26], and vapor sensors [27–29]. Unlike electronic amplification, parametric amplification has an inherent advantage of providing higher sensitivity in MEMS sensor systems, as it amplifies the sensor signal without adding any extra electronic noise to the circuit.

In this paper, we report the design, fabrication, and testing of a new type of low power, batch-fabricatable, parametrically amplified, microcantilever-based humidity sensor with improved sensitivity. This article expands on a proof of concept presented earlier [29]. Extensive characterization of the sensor response has been presented in this article, along with dynamic response testing and comparison to a commercially available sensor. Additionally, a relevant analysis of the sensor output and a mathematical model describing the sensor action is also presented, along with a study on the sorption kinetics of the device.

## 2. Device Structure and Operation

A unit cell of the LACM sensor is shown in Figure 1a. The device consists of a suspended microcantilever beam (electrode 2) asymmetrically coated on top with a sensing polymer (polyimide) and flanked on the sides by two stationary electrodes (1 and 3). When the device is exposed to an analyte vapor, the polyimide absorbs the gas and swells. This exerts a bending moment,  $M_{RH}$ , on the structural beam causing it to deflect to one side (Figure 1b). Unlike conventional polymer-based microcantilever sensors, which measure the out-of-plane deflection of the cantilever [30], the LACM sensor measures the in-plane deflection of the sensing cantilever by forming two parallel plate variable capacitors between the central finger and the adjacent electrodes, as shown below. Our devices are appropriately designed to make the out-of-plane stiffness much higher than the in-plane spring constant. A planar design allows multiple unit cell structures to be united in parallel to increase the total output signal from the sensor (Figure 1c) while maintaining compatibility with conventional CMOS processes suitable for low power, high sensitivity water vapor sensors for application in IoT frameworks.

Furthermore, parametric amplification of the output signal is achieved by applying a symmetric DC bias voltage to both the flanking electrodes (1 and 3) with respect to the central suspended electrode (2) to improve the vapor-concentration to displacement sensitivity of the device (Figure 1d). In this work, the single side capacitance measurements for the device have been reported. Theoretically, the sensor performance can be further improved by measuring a differential capacitance between the two sides while also eliminating common mode parasitics.

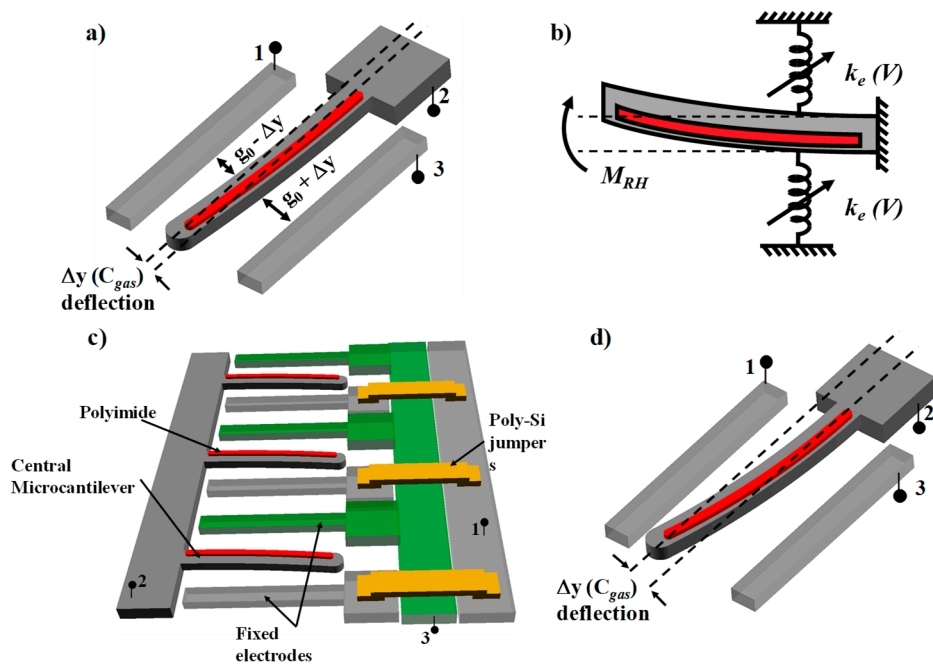


**Figure 1.** (a) Unit cell of the LACM humidity sensor. (b) Mechanical equivalent of the device when subjected to a change in relative humidity. (c) Array structure of parallel LACM unit cells. (d) Use of parametric amplification to magnify the deflection sensitivity of the central microcantilever.

### 2.1. Electrostatic Spring Softening

Parametric amplification induced spring softening in the mechanical domain has been extensively studied to tune the resonant frequency of the MEMS structures [31–33] and to produce large-amplitude deflections in microstructures [26,34]. In the LACM sensor, when a DC bias voltage is applied to the electrodes 1 and 3 with respect to electrode 2, the non-linearity of the electrostatic forces acting on the central cantilever beam results in the reduction of the effective spring constant of the central cantilever. Mathematically, electrostatic spring softening of micromechanical systems can be observed by minimizing the total energy ( $U_T$ ) function of the system:

$$U_T = U_{EL} + U_M \quad (1)$$

where  $U_{EL}$  is the electrostatic energy stored in the capacitors of the system and  $U_M$  is the mechanical energy stored in the deformed microcantilever beam. For a microcantilever beam deflecting laterally between two electrodes, as shown in Figure 1, the respective energies can be written as:

$$U_{EL} = \frac{-\varepsilon AV_b^2}{2} \left( \frac{1}{g_0 + \Delta y} + \frac{1}{g_0 - \Delta y} \right) \quad (2)$$

$$U_M = \frac{k_0 \Delta y^2}{2} \quad (3)$$

where  $g_0$  is the initial gap between the electrodes,  $\Delta y$  is the tip deflection of the central beam due to absorption induced polymer swelling,  $V_b$  is the applied DC bias voltage,  $A$  is the overlap area of the capacitor,  $\varepsilon$  is the permittivity, and  $k_0$  is the lateral spring constant of the central finger when no bias is applied. For  $\frac{\Delta y}{g_0} \ll 1$ , the total energy of the system can be written as:

$$U_T = \frac{1}{2} k_0 \Delta y^2 - \left[ \frac{\varepsilon AV_b^2}{g_0} \right] \left( \frac{1}{1 - \left( \frac{\Delta y}{g_0} \right)^2} \right) \quad (4)$$

$$U_T = \frac{1}{2}k_0 \left[ \Delta y^2 - \left( \frac{2\epsilon AV_b^2}{k_0 g_0} \right) \left( 1 + \left( \frac{\Delta y}{g_0} \right)^2 - \left( \frac{\Delta y}{g_0} \right)^4 + \dots \right) \right] \tag{5}$$

$$U_T \cong \frac{1}{2}k_0 \underbrace{\left[ 1 - \left( \frac{2\epsilon AV_b^2}{k_0 g_0^3} \right) \right]}_{k(M)} \Delta y^2 + h.o.t \tag{6}$$

For  $V_p = \sqrt{\frac{k_0 g_0^3}{2\epsilon A}}$ , which is the symmetrically-biased pull-in voltage for the structure, the effective softened spring constant  $k(M)$ , can be written as:

$$k(M) = \frac{k_0}{M} \text{ where, } M = \frac{1}{\left( 1 - \frac{V_b^2}{V_p^2} \right)} \tag{7}$$

For example, Figure 2a shows the total energy of a system with  $k_0 = 3.7 \text{ Nm}^{-1}$  and  $V_p = 35.4 \text{ V}$  without DC bias ( $V_1 = 0 \text{ V}$ ) and, when DC voltage bias ( $V_2 = 18 \text{ V}$  and  $V_3 = 28 \text{ V}$ ) is applied to induce parametric amplification, as a function of normalized beam deflection. As the magnitude of the applied voltage bias is increased, the system becomes progressively unstable due to the shallowing of the local energy minima. Since  $k(M) < k_0$ , the output signal is magnified by a voltage-dependent magnification factor,  $M$ , as shown in Figure 2b. Note that the above derivation is an approximation as it assumes  $\Delta y$  to be the uniform change in the gap across the entire length of the beam. Though parametric amplification can be used to obtain signal magnification, it is important to note that operating very close to the pull-in voltage (very high gains) would require additional voltage stabilization electronics to prevent the beam from latching sideways. Additionally, inducing higher degrees of spring softening does limit the operational range of the sensor because the range of stable deflections for the central beam before pull-in decreases, as voltage bias is increased.

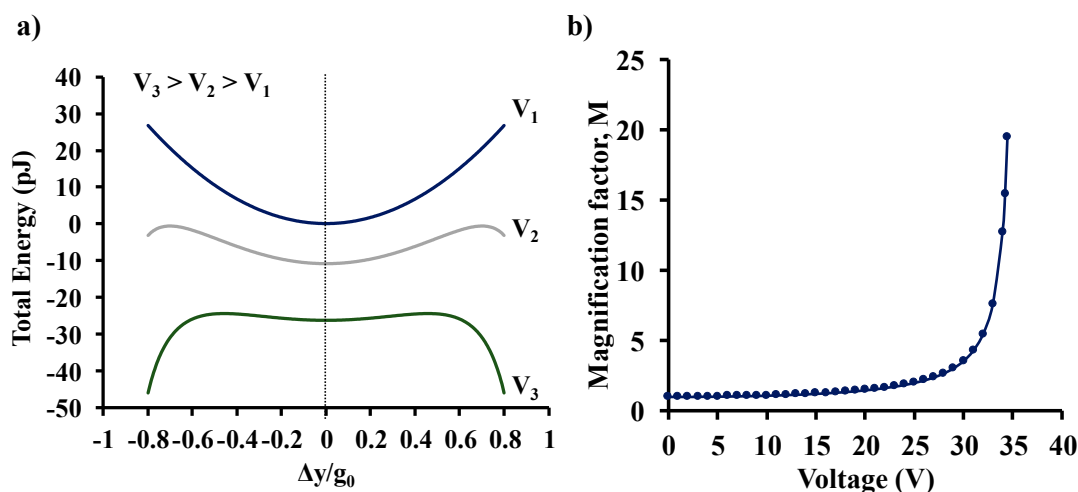
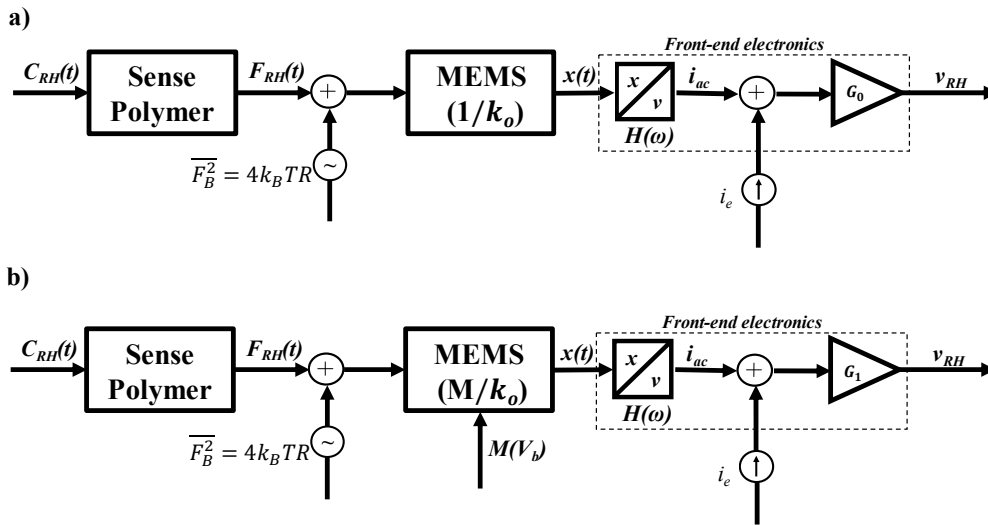


Figure 2. Schematic of the (a) total energy of the system during parametric amplification, and (b) magnification factor  $M$  as a function of the applied voltage.

### 2.2. Noise Analysis and Signal-to-Noise Ratio

The noise of the system originates from both the mechanical-thermal noise [35,36] of the deflecting beam and the noise of the C/V converter operational amplifiers [37]. In our device, we convert the stress caused by the RH absorption ( $F_{RH}$ ) into a mechanical deflection, which translates into a variable, and RH dependent capacitance, mediated through the beam spring constant  $k(M) = k_0/M$ , where  $M$  is

the bias-dependent magnification factor. We use high-gain op-amps to amplify and read the sensor capacitance [38], as illustrated in the schematic of Figure 3a below.



**Figure 3.** (a) Schematic of the sensor system at zero bias with default spring constant  $k_0$  (b) with parametric amplification (near-Brownian noise is limited).

The capacitance change indicative of the vapor concentration signal is first converted to an AC current with  $i_{ac} = j\omega C(RH) \cdot V_o$ , where  $V_o$  is the amplitude of a sinusoidal AC voltage of angular frequency  $\omega$  placed across the capacitor. The AC current is finally converted to an output voltage using a high-gain op-amp of transconductance  $G_o$ . The noise of the system is calculated by the introduction of two noise sources: (1) a mechanical noise acting on the beam with spectral density [35,39]:

$$F_B = \sqrt{4k_B TR} \left[ N / \sqrt{\text{Hz}} \right] \quad (8)$$

which is only dependent on the Boltzmann constant  $k_B$ , temperature  $T$ , and viscous damping coefficient  $R$  of the system, as described previously in a viscous damping environment (air) and at low pressures [36]. Therefore, the noise force on the MEMS device is completely independent of the bias induced spring softening used in the LACM sensor. (2) The electronic noise current source  $i_e^2$ , which is introduced at the input of the transconductance amplifier. The output noise for this system is thus:

$$\overline{v_o^2}(k_o) = G_o^2 \left( \omega^2 V_o^2 F^2 \frac{\overline{F_B^2}}{k(M)^2} + \overline{i_e^2} \right) = G_o^2 \left( \omega^2 V_o^2 F^2 \frac{\overline{F_B^2}}{k_o^2} + \overline{i_e^2} \right) = G_o^2 \left( H^2(\omega) \cdot \frac{\overline{F_B^2}}{k_o^2} + \overline{i_e^2} \right) \quad (9)$$

where

$$H^2(\omega) = \omega^2 V_o^2 F^2, \quad F^2 = \left( \frac{dC}{dF_B} \right)^2 \quad (10)$$

Since the deterministic signal  $v_{RH}^2 = H^2(\omega) \cdot \frac{F_{RH}^2}{k_o^2} \cdot G_o^2$ , where  $F_{RH}$  is the equivalent RH-driven force, the signal to noise ratio is thus given by:

$$SNR_o = \frac{\frac{F_{RH}}{k_o} \cdot H(\omega)}{\sqrt{\frac{F_B^2}{k_o^2} \cdot H^2(\omega) + i_e^2}} = \frac{\left( \frac{F_{RH}}{F_B} \right)}{\sqrt{1 + \left( \frac{k_o^2}{H^2(\omega) \cdot F_B^2} \right) \cdot i_e^2}} \dots = \frac{SNR_{max}}{\sqrt{1 + \left( \frac{k_o^2}{H^2(\omega) \cdot F_B^2} \right) \cdot i_e^2}} \quad (11)$$

It is evident that the SNR is independent of transconductance  $G_o$ . Equation (11) also tells us that any electromechanical effect that lowers  $k_o$  will result in a higher SNR. In our device, this can

be achieved with the bias-induced spring softening gain  $M$ , as shown in the schematic of Figure 3b, such that:

$$SNR(M) = \frac{SNR_{max}}{\sqrt{1 + \frac{\left(\frac{SNR_{max}}{SNR_0}\right)^2 - 1}{M^2}}} \quad (12)$$

The SNR is improved for  $M > 1$  essentially because the spring softening effect gain is noiseless, thus moving the electronic noise closer to the amplified output.

### 2.3. Sensor Response Model

The LACM sensor is essentially a humidity-dependent variable and parallel-plate capacitor. When the device is exposed to humidity, the sensing polymer swells after absorbing the water vapor. Since the polymer is asymmetrically patterned and constrained to the silicon cantilever beam, the swelling generates surface stress [40], which results in the bending of the cantilever beam towards one side. This results in a change in the measured capacitance of the device. The amount of cantilever bending and, therefore, the capacitance change is directly proportional to the swelled induced surface stress and inversely proportional to the effective spring constant of the device given by Equation (7). This can be mathematically described by a modified form of Stoney's equation as given by Godin et al. [41].

For small displacements of the central cantilever beam, the normalized change in capacitance can be written as:

$$\frac{\Delta C}{C} = (A_0) \left[ \frac{(1-\nu)l^2}{g_0 E_{Si} w^2} \cdot \frac{1}{\left(1 - \frac{V^2}{V_p^2}\right)} \cdot \beta_p \cdot C_{RH} \right] + B_0 \quad (13)$$

where  $\nu$  = Poisson's ratio of Silicon,  $l$  = length of central cantilever beam,  $g_0$  = initial air-gap between electrodes,  $E_{Si}$  = Young's Modulus of Silicon,  $w$  = width of central cantilever beam,  $V$  = applied voltage bias to induce spring softening,  $V_p$  = symmetrically-biased pull-in voltage of beam,  $\beta_p$  = fitting parameter proportional to the swelling-induced surface stress generated by the polyimide, and  $C_{RH}$  is the relative humidity of the chamber.  $A_0$  and  $B_0$  are dimensionless fitting parameters.

### 2.4. 2-Level Electrical Interconnects

The laterally deflecting and planar design of the LACM sensor allows the connection of multiple unit cells in parallel in order to further increase the output of the sensor. Since each microcantilever is flanked on the two sides by electrically isolated anchored electrodes, it is necessary to have a 2-level electrical connection arrangement in the device. In the LACM sensor array, this is done by fabricating jumpers out of doped poly-Si, as shown in Figure 1c. The detailed fabrication procedure is described in the following sections. The jumper arrangement eliminates the needs for wire bonds to connect multiple devices, thus keeping the fabrication process simple.

## 3. Fabrication and Imaging

### 3.1. Device Fabrication

Figure 4a–l shows a simplified fabrication procedure of the device. The process starts by depositing 250 nm of low-stress silicon nitride using a Low Pressure Chemical Vapor Deposition (LPCVD) process over Silicon-on-Insulator (SOI) wafers with a 30  $\mu\text{m}$  thick device layer and a 2  $\mu\text{m}$  thick buried oxide layer, as shown in Figure 4a. The nitride layer is patterned using conventional UV photolithography width and then etched using  $\text{CF}_4/\text{O}_2$  RIE. The device layer of the SOI wafer is then etched using Deep Reactive Ion Etching (DRIE) to form the fingers (Figure 4b). A low-frequency RF source (380 kHz) is used for this process to avoid footing and prevent premature release of the device. The photoresist is then removed using acetone, and a pre-furnace clean is performed. A 100 nm thin layer of LPCVD silicon nitride is then deposited on the wafer, and a blanket  $\text{CF}_4/\text{O}_2$  RIE etch is done. This ensures

that the nitride remains only on the sidewalls of the etched fingers (Figure 4c). A 4  $\mu\text{m}$  thick layer of sacrificial LPCVD Phosphosilicate glass (PSG) is then deposited on the wafer and annealed in an  $\text{N}_2$  environment at 1050  $^\circ\text{C}$  to reflow the PSG. The thickness of the PSG is then reduced to  $\sim 2 \mu\text{m}$  using a blanket RIE etch on the wafer. This deposition-reflow and etch back process is repeated until the etched gaps between different fingers are entirely sealed (Figure 4d) due to the cusping effect in an LPCVD process, thus allowing further processing of the wafer [42,43]. The sacrificial PSG and the underlying nitride are then patterned using photolithography and RIE to create anchors (Figure 4e) for poly-Si jumpers and the anti-stiction micro-staple pins. A 4  $\mu\text{m}$  thick layer of poly-Si is then deposited using the LPCVD process. This layer is then doped using phosphorus solid-source doping and annealed at 1050  $^\circ\text{C}$  for 2 h (Figure 4f). A 200 nm thick layer of Cr is then deposited over the wafer using DC-sputtering and patterned using a wet etchant to form the metal contact and jumpers (Figure 4g). The wafer is then cleaned, and the anti-stiction features are patterned (Figure 4h). This step also forms the poly-Si jumpers and contact pads, with the previously patterned Cr metal acting as an etch mask. The PSG on the central finger is then patterned and etched to create windows (Figure 4i) to allow deposition and anchoring of the sensing polymer to the device. We use HD-4104 polyimide [44] as a water vapor sensing material. The polyimide is spin-coated on the sample at 3000 rpm and soft-baked at 90  $^\circ\text{C}$  for 2 min, followed by 100  $^\circ\text{C}$  for 2 min. The polymer is then cured at 300  $^\circ\text{C}$  in an oven with  $\text{N}_2$  environment for 3 h. A commercially available Polyimide adhesion promoter, VM-651, is applied to the sample before spin-coating to improve the adhesion of the polyimide to the substrate and to prevent any delamination during the Buffered Oxide Etch (BOE) release procedure. The obtained thickness of the polyimide was  $\sim 3.35 \mu\text{m}$ , which was measured using a Tencor P-10 Profilometer. A 200 nm thick Al layer is then sputtered on the polyimide and then patterned asymmetrically on the central finger using wet etching to act as a hard mask. The polyimide is then etched using  $\text{O}_2$  plasma (Figure 4j) in an Oxford 100 ICP etcher to obtain a 7  $\mu\text{m}$  wide polymer patch. The devices are then diced, and the chips are released in BOE for 160 min with constant stirring (Figure 4k). The etching time was determined by running a few trial samples for different etch times to confirm device release and determine the undercut rate. The chips are finally rinsed thoroughly in DI water followed by methanol and allowed to air dry.

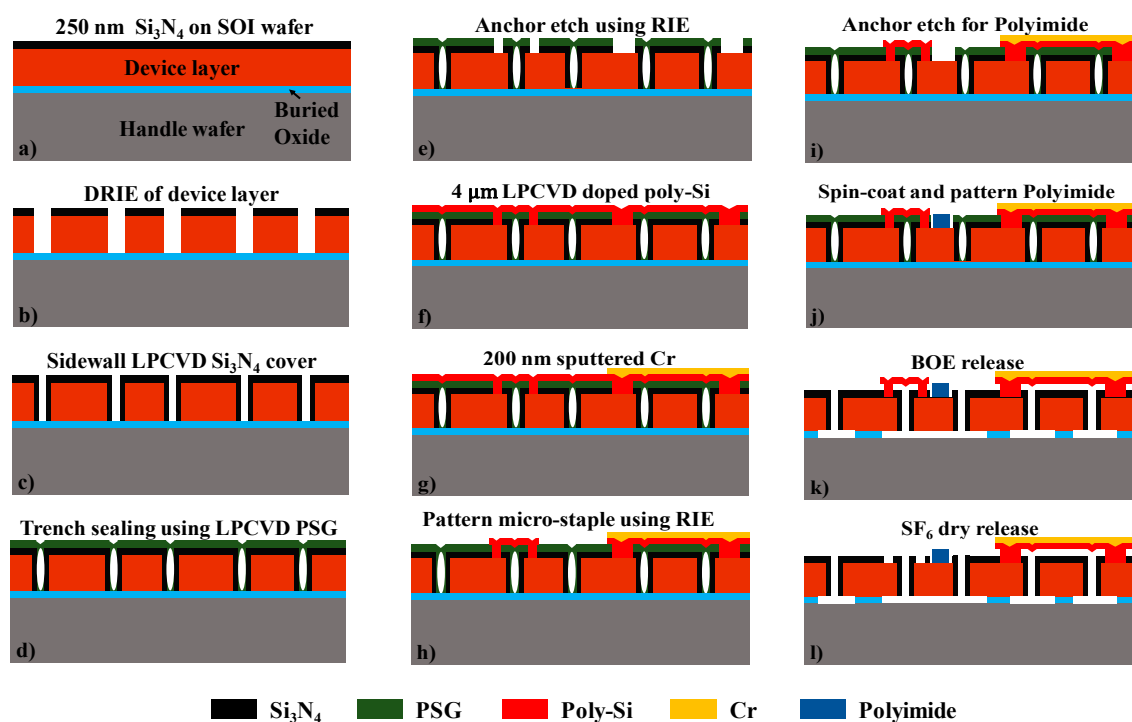


Figure 4. Simplified fabrication procedure of the device.

### 3.2. Stiction Suppression

Stiction is one of the main modes of failure in MEMS devices [45]. Device failure due to stiction occurs when suspended MEMS structures, such as cantilevers, plates, or beams, adhere to the substrate or adjacent features due to lack of sufficient restoring force when subjected to strong capillary forces. Typically, capillary forces arise during the device fabrication and cleaning due to the surface tension of water when the sample is allowed to dry. Various methods have been previously used to prevent stiction due to surface tension [45–47]. In the LACM device, a different method which utilizes ‘micro staple-pins’ that hold the released cantilever in place during a wet release procedure, has been utilized. The staples are made out of thin poly-Si that can be dry etched, thus eliminating the need for complex and expensive anti-stiction processes.

A very short  $\text{SF}_6$  etch is finally performed on the devices to etch away the anti-stiction micro-staples and release the fingers (Figure 4l). Any unwanted etching on the side wall of the fingers is prevented by the thin  $\text{Si}_3\text{N}_4$  film that is deposited over the finger before PSG sealing.

### 3.3. Imaging

High-resolution Scanning Electron Microscope (SEM) imaging of the device was done on an FEI Quanta 600 SEM at an accelerating voltage of 20.0 kV to verify the fabricated device structure, as shown in Figure 5a–c. Figure 5a shows the fabricated device array with the poly-Si jumpers acting as the second level of electrical connections, which are shown in the zoomed in image (Figure 5b). Only the central finger is released during the timed BOE wet etch, as the flanking electrodes are much wider and, therefore, stay anchored. Zoomed-in image of the central finger is visible in Figure 5c, showing the asymmetrically patterned polyimide on the movable beam and the anti-stiction micro-staple pins clamping the central finger to the side electrodes after wet release. The fabricated devices were  $900\ \mu\text{m}$  long, and the suspended beams were  $13.3\ \mu\text{m}$  wide. The air-gap measured between the suspended beam and the side electrode was  $4.75\ \mu\text{m}$ . The symmetrically-biased pull-in voltage was calculated to be  $\sim 29.5\ \text{V}$ . The fabricated device had 15 unit cells connected in a parallel circuit.

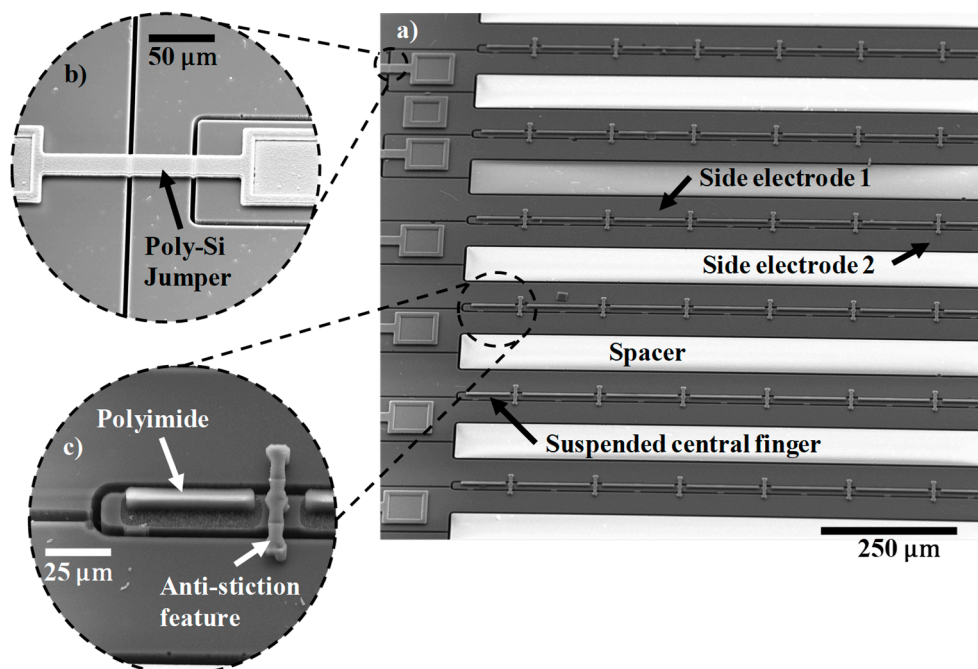


**Figure 5.** (a) LACM sensor array; (b) zoomed-in image of a poly-Si jumper over etched trenches acting as the second level of electrical connections; (c) magnified view of a suspended central finger with asymmetrically patterned polyimide and anti-stiction micro-staple holder.



## 4. Testing and Characterization

### 4.1. Test Setup

The sensor electrical testing was done at a probe station enclosed in a metallic box to create a localized environment for vapor testing. The enclosing box was grounded to reduce outside interference and noise during measurement. The device capacitance was measured using a Keithley 4200A-SCS CVU that was connected to the probe station at 1 MHz frequency using a 30 mV AC signal. The base capacitance of the device was measured to be 270 fF. The chamber was flushed with N<sub>2</sub> gas before testing, and a commercial humidifier that was placed outside was used to humidify the chamber. The relative humidity (RH) of the chamber was monitored using a commercially available BME-280 [48] chip connected to an Arduino Uno board, which reported the chamber humidity to a computer. Dehumidification of the chamber was done by purging the test chamber with N<sub>2</sub> while evacuating the chamber using an in-house vacuum line.

### 4.2. Sensor Action and Humidity Response

Figure 6a shows the normalized response of the sensor as a function of varying water-vapor concentration at different biasing voltages. Sensor capacitance decreases when operated at no-bias voltage, which we believe is due to a reduction in overlap area because of undesirable out-of-plane downward deflection of the central cantilever beam when exposed to increasing humidity. Application of a small DC bias voltage results in stiffening of the out-of-plane spring constant of the central finger due to induced electrostatic levitation, as described by Tang et al. [49], which prevents out-of-plane deflection. Figure 6b shows the sensor characteristics at different relative humidity levels as a function of varying bias voltage, indicating sensor output amplification as the bias voltage is increased at a constant humidity level. An ~11-fold magnification of sensor response was observed for a bias voltage of 28 V, compared to when a low bias (5 V) voltage was used at 40.83%RH, as shown in Figure 7. The noise floor was experimentally measured to be approximately the same (~400 aF), both with and without parametric amplification corresponding to a noise current of 75.4 pA and dominated by electronic noise in the setup and the capacitance meter. Figure 8 shows the dynamic response of the device when exposed to a gradual change in relative humidity from 20–90%, and operated at a bias voltage of 28 V. Highly repeatable device performance was observed, and no sensor saturation was seen, as shown in Figure 8a. Figure 8b shows the continuous operation of the sensor over five cycles of chamber humidification/dehumidification and shows near zero baseline drift.

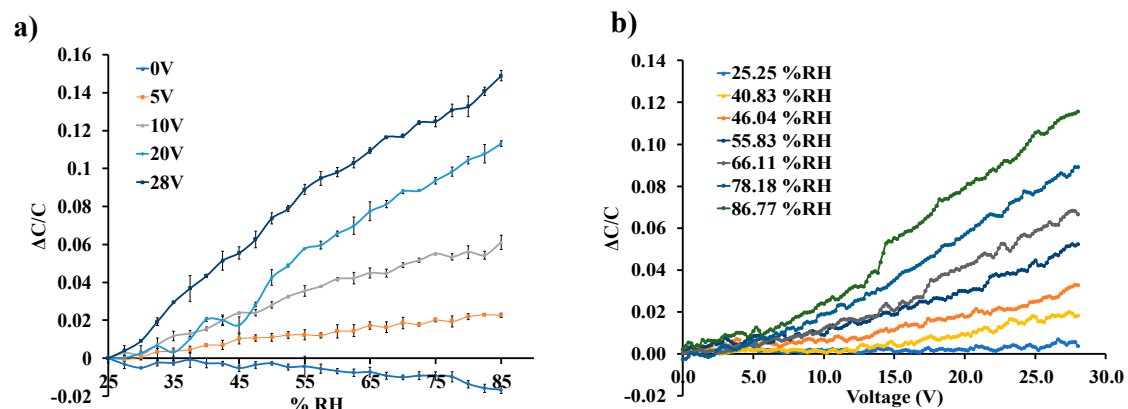


**Figure 6.** (a) Sensor response to varying %RH levels at different DC bias voltage; (b) sensor response to a varying bias voltage at different %RH levels.

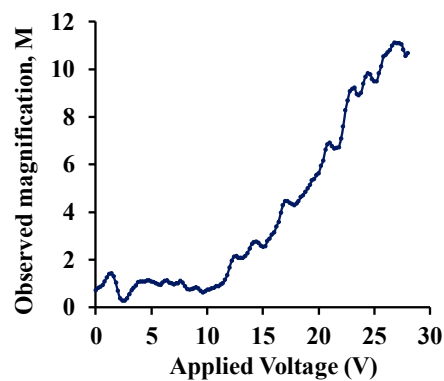


**Figure 7.** Observed sensor output magnification as a function of applied bias voltage at constant relative humidity.

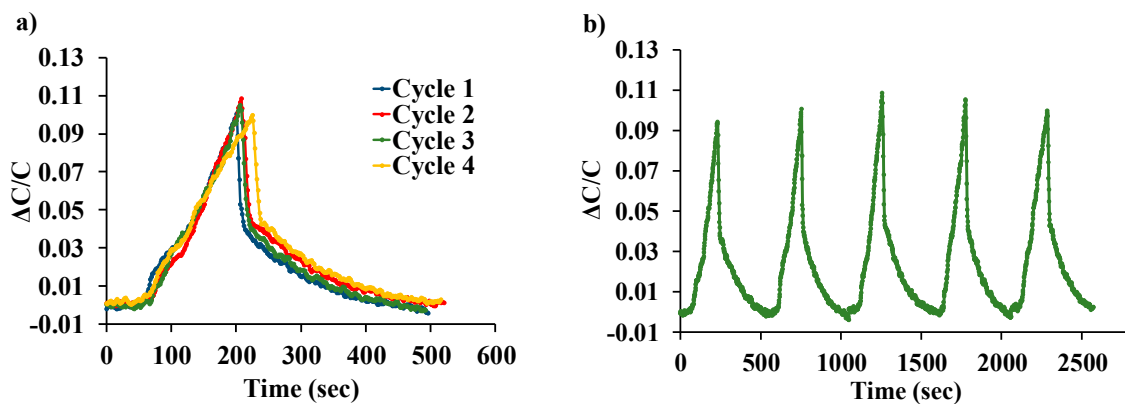


**Figure 8.** (a) Repeatability of LACM sensor tested over four cycles. (b) Sensor output over five consecutive cycles of exposure and removal of humidity.

#### 4.3. Model Fitting

Figure 9a shows the equivalent electrical circuit of the LACM sensor. The humidity response of the device was curve-fitted to Equation (13), and the plot is shown in Figure 9b. Parameter extraction revealed the mean value of  $\beta_p \sim 0.114 \text{ mN}\cdot\text{m}^{-1}$  per ppm of water vapor, and the value of the fitting parameters  $A_0$  and  $B_0$  ranged from 2.5 to 12 and  $-0.06$  to  $-0.01$ , respectively. The root-mean-square error was found to be 0.1%, 0.39%, and, 0.52% for applied bias voltages 5 V, 20 V, and 28 V, respectively.

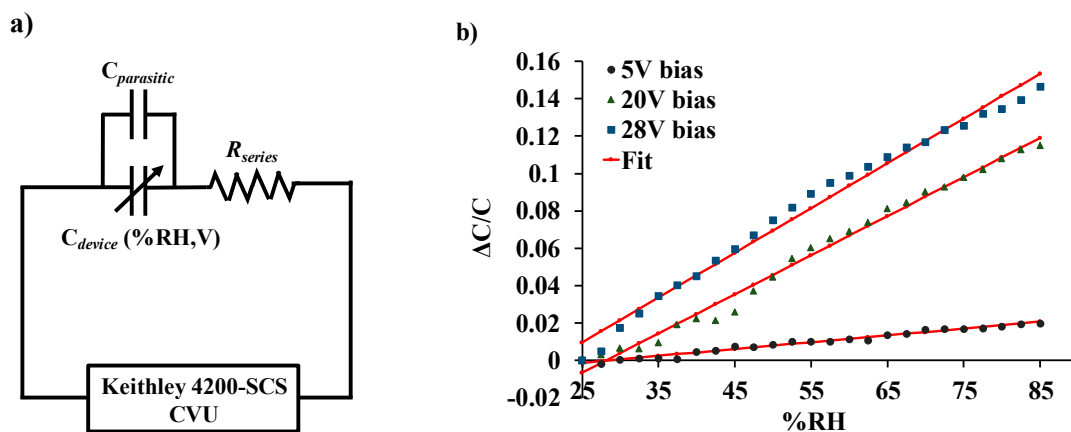


**Figure 9.** (a) Equivalent electrical representation of the LACM sensor. (b) Normalized change in capacitance of the sensor curve fitted to Equation (13).

#### 4.4. Absorption-Desorption Kinetics

The dynamic response of the device is dependent on the moisture absorption induced swelling of the polyimide on the central cantilever beam. This type of behavior can be explained by a modified version of Fick's second law of diffusion. The performance of the LACM sensor can be effectively modeled as described by Sikame Tagne [50]. The desorption kinetics of the sensor is considered as the gradual desorption of water molecules back into the atmosphere and modeled using the Polanyi–Wigner equation [51]. The curve fitted normalized change in capacitance is shown in Figure 10a when the humidity is increased from 25–85% and then decreased back to 25%. Additionally, Figure 10b compares the normalized device response to that of a commercially available BME-280 [48] reference sensor chip. It can be observed from the plot that the LACM sensor closely follows the response of the reference chip, which has a response time of 1 s [48] with both the sensors reaching their maximum output at the same time.

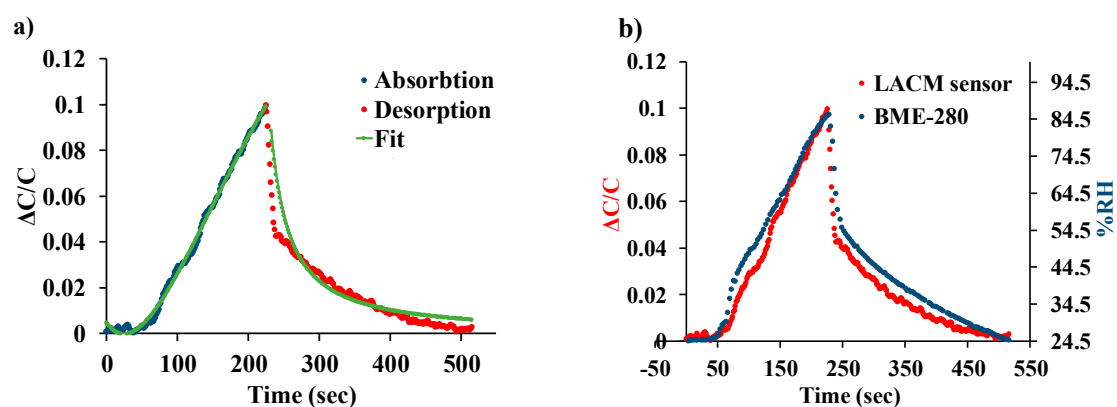


**Figure 10.** (a) Dynamic response of the LACM sensor curve fitted to Fick's second law and the Polanyi–Wigner equation. (b) Comparison of the LACM sensor performance to a commercially available BME-280 reference chip.

## 5. Conclusions

We presented the design, fabrication, and response of a batch-fabricated capacitive polymer-based humidity sensor based on mechanical leveraging and parametric amplification. The device exploits the electrostatic lateral instability of MEMS structures to achieve a noiseless intrinsic gain, which helps in achieving a better SNR. An  $\sim 11$ -fold magnification in sensor output was achieved by applying a 28 V DC bias voltage to the device at constant water vapor concentration due to spring softening. We demonstrated an unassisted and completely recoverable change of 11% in capacitance value when subjected to a humidity change from 25–85%. The dynamic response of the sensor was also characterized, and the sensor showed a comparable response to a commercially available reference chip with  $\sim 1$  s response time. A mathematical model to accurately describe the sensor action and sensor dynamics has also been presented. Such a sensor is an excellent candidate for a low-power, low-cost, and sensitive vapor-sensor for applications in IoT based frameworks. Future work would involve using the LACM sensor for the detection of other analytes, such as volatile organic compounds, and addressing the issue of temperature sensitivity of this device due to its bimorph type structure.

**Author Contributions:** R.L. designed, fabricated and tested all devices as well as performed characterization of the LACM sensor, wrote and proofread the manuscript. A.B. assisted in device testing, mathematical modeling, manuscript preparation, and proofreading. A.M. and M.K. assisted in manuscript proofreading. H.K. helped in the experimental setup. C.H.M. helped in concept inception, device testing, fabrication, and analysis of results as well as the preparation and proofreading of the manuscript.

**Funding:** This research received no external funding.

**Acknowledgments:** The authors would like to thank the staff at the University of Utah Nanofab and, the Surface Analysis Lab for their assistance in fabricating and imaging the LACM sensor.

**Conflicts of Interest:** The authors declare no conflict of interest the results.

## References

1. Yamazoe, N.; Shimizu, Y. Humidity sensors: Principles and applications. *Sens. Actuators* **1986**, *10*, 379–398. [[CrossRef](#)]
2. Chen, Z.; Lu, C. Humidity sensors: A review of materials and mechanisms. *Sens. Lett.* **2005**. [[CrossRef](#)]
3. Rittersma, Z.M.M. Recent achievements in miniaturised humidity sensors—A review of transduction techniques. *Sens. Actuators A Phys.* **2002**, *96*, 196–210. [[CrossRef](#)]
4. Bariáin, C.; Matías, I.R.; Arregui, F.J.; López-Amo, M. Optical fiber humidity sensor based on a tapered fiber coated with agarose gel. *Sens. Actuators B Chem.* **2000**. [[CrossRef](#)]
5. Penza, M.; Cassano, G. Relative humidity sensing by PVA-coated dual resonator SAW oscillator. *Sens. Actuators B Chem.* **2000**. [[CrossRef](#)]
6. Banerjee, A.; Likhite, R.; Kim, H.; Mastrangelo, C.H. Quantum Tunneling Hygrometer with Temperature Stabilized Nanometer Gap. Available online: <http://arxiv.org/abs/1906.02451> (accessed on 7 June 2019).
7. Fenner, R.; Zdankiewicz, E. Micromachined water vapor sensors: A review of sensing technologies. *IEEE Sens. J.* **2001**. [[CrossRef](#)]
8. Why Control Humidity in a Cleanroom? Solid State Technology. Available online: <https://electroiq.com/2003/10/why-control-humidity-in-a-cleanroom/> (accessed on 6 June 2019).
9. Wang, N.; Zhang, N.; Wang, M. Wireless sensors in agriculture and food industry—Recent development and future perspective. *Comput. Electron. Agric.* **2006**. [[CrossRef](#)]
10. Balaras, C.A.; Dascalaki, E.; Gaglia, A. HVAC and indoor thermal conditions in hospital operating rooms. *Energy Build.* **2007**. [[CrossRef](#)]
11. Zhao, J.C.; Zhang, J.F.; Feng, Y.; Guo, J.X. The study and application of the IOT technology in agriculture. In Proceedings of the 3rd IEEE International Conference on Computer Science and Information Technology (ICCSIT 2010), Chendu, China, 9–11 July 2010. [[CrossRef](#)]
12. Banerjee, A.; Ghosh, T.; Likhite, R.; Hasan, N.; Kim, H.; Mastrangelo, C.H. Electrical detection of proteins using batch-fabricated vertical metal nanogap break-junctions. In Proceedings of the 20th International Conference on Miniaturized Systems for Chemistry and Life Sciences (MicroTAS 2016), Dublin, Ireland, 9–13 October 2016.
13. Banerjee, A.; Farhoudi, N.; Ghosh, C.; Mastrangelo, C.H.; Kim, H.; Broadbent, S.J.; Looper, R. Picowatt gas sensing and resistance switching in tunneling nano-gap electrodes. In Proceedings of the IEEE Sensors, Glasgow, Scotland, 29 October–1 November 2017. [[CrossRef](#)]
14. Banerjee, A.; Khan, S.-U.H.; Broadbent, S.; Likhite, R.; Looper, R.; Kim, H.; Mastrangelo, C.H. Batch-fabricated  $\alpha$ -Si assisted nanogap tunneling junctions. *Nanomaterials* **2019**, *9*, 727. [[CrossRef](#)]
15. Traversa, E. Ceramic sensors for humidity detection: The state-of-the-art and future developments. *Sens. Actuators B Chem.* **1995**. [[CrossRef](#)]
16. Sakai, Y.; Sadaoka, Y.; Matsuguchi, M. Humidity sensors based on polymer thin films. *Sens. Actuators B Chem.* **1996**. [[CrossRef](#)]
17. Chatzandroulis, S.; Tserepi, A.; Goustouridis, D.; Normand, P.; Tsoukalas, D. Fabrication of single crystal Si cantilevers using a dry release process and application in a capacitive-type humidity sensor. *Microelectron. Eng.* **2002**, *61*, 955–961. [[CrossRef](#)]
18. Lee, C.Y.; Lee, G.B. Micromachine-based humidity sensors with integrated temperature sensors for signal drift compensation. *J. Micromech. Microeng.* **2003**. [[CrossRef](#)]
19. Thompson, M.J.; Horsley, D.A. Parametrically Amplified MEMS Magnetometer. In Proceedings of the Transducers 2009—15th International Conference Solid-State Sensors, Actuators Microsystems, Denver, CO, USA, 21–25 June 2009. [[CrossRef](#)]
20. Baselt, D.R.; Fruhberger, B.; Klaassen, E.; Cemalovic, S.; Britton, C.L.; Patel, S.V.; Mlsna, T.E.; McCorkle, D.; Warmack, B. Design and performance of a microcantilever-based hydrogen sensor. *Sens. Actuators B Chem.* **2003**. [[CrossRef](#)]
21. Likhite, R.; Banerjee, A.; Kim, H.; Mastrangelo, C.H. Self-Leveling Micromechanical Gas Sensors. In Proceedings of the IEEE Sensors, New Delhi, India, 28–31 October 2018; pp. 1–4. [[CrossRef](#)]

22. Álvarez, M.; Carrascosa, L.G.; Moreno, M.; Calle, A.; Zaballos, Á.; Lechuga, L.M.; Martínez-A, C.; Tamayo, J. Nanomechanics of the formation of DNA self-assembled monolayers and hybridization on microcantilevers. *Langmuir* **2004**. [CrossRef] [PubMed]
23. Hansen, K.M.; Thundat, T. Microcantilever biosensors. *Methods* **2005**, *37*, 57–64. [CrossRef] [PubMed]
24. Yang, Y.; Ji, H.F.; Thundat, T. Nerve agents detection using a Cu<sup>2+</sup>/L-cysteine bilayer-coated microcantilever. *J. Am. Chem. Soc.* **2003**. [CrossRef]
25. Sharma, M.; Sarraf, E.H.; Baskaran, R.; Cretu, E. Parametric resonance: Amplification and damping in MEMS gyroscopes. *Sens. Actuators A Phys.* **2012**, *177*, 79–86. [CrossRef]
26. Droogendijk, H.; Bruinink, C.M.; Sanders, R.G.P.; Dagamseh, A.M.K.; Wiegerink, R.J.; Krijnen, G.J.M. Improving the performance of biomimetic hair-flow sensors by electrostatic spring softening. *J. Micromechanics Microengineering*. **2012**, *22*, 065026. [CrossRef]
27. Banerjee; Pandey, S.S.; Banerjee, N.; Hasan, N.; Mastrangelo, C.H. A Milli-volt triggered MEMS Paddle Switch. In Proceedings of the 2015 IEEE Sensors, Busa, Korea, 1–4 November 2015. [CrossRef]
28. Pandey, S.S.; Banerjee, N.; Banerjee, A.; Hasan, N.; Kim, H.; Mastrangelo, C.H. High-sensitivity Parametrically Amplified Chemo-Mechanical Vapor Sensors. In Proceedings of the 2015 IEEE Sensors, Busa, Korea, 1–4 November 2015. [CrossRef]
29. Likhite, R.; Pandey, S.S.; Banerjee, A.; Kim, H.; Mastrangelo, C.H. Amplified chemomechanical comb gas sensor. In Proceedings of the IEEE Sensors, Orlando, FL, USA, 30 October–3 November 2016; pp. 1–3. [CrossRef]
30. Singamaneni, S.; McConney, M.E.; LeMieux, M.C.; Jiang, H.; Enlow, J.O.; Bunning, T.J.; Naik, R.R.; Tsukruk, V.V. Polymer-silicon flexible structures for fast chemical vapor detection. *Adv. Mater.* **2007**. [CrossRef]
31. Zhang, W.; Meng, G. Nonlinear dynamical system of micro-cantilever under combined parametric and forcing excitations in MEMS. *Sens. Actuators A Phys.* **2005**, *119*, 291–299. [CrossRef]
32. Elshurafa, A.M.; Khirallah, K.; Tawfik, H.H.; Emira, A.; Aziz, A.K.S.A.; Sedky, S.M. Nonlinear dynamics of spring softening and hardening in folded-mems comb drive resonators. *J. Microelectromech. Syst.* **2011**. [CrossRef]
33. Torun, H.; Sarangapani, K.K.; Degertekin, F.L. Spring constant tuning of active atomic force microscope probes using electrostatic spring softening effect. *Appl. Phys. Lett.* **2007**. [CrossRef]
34. Krylov, S.; Gerson, Y.; Nachmias, T.; Keren, U. Excitation of large-amplitude parametric resonance by the mechanical stiffness modulation of a microstructure. *J. Micromech. Microeng.* **2010**, *20*, 015041. [CrossRef]
35. Gabrielson, T.B. Mechanical-Thermal Noise in Micromachined Acoustic and Vibration Sensors. *IEEE Trans. Electron. Devices* **1993**. [CrossRef]
36. Cleland, A.N.; Roukes, M.L. Noise processes in nanomechanical resonators. *J. Appl. Phys.* **2002**. [CrossRef]
37. Gray, P.R. Analysis and Design of Analog Integrated Circuits. Available online: <https://www.wiley.com/en-us/Analysis+and+Design+of+Analog+Integrated+Circuits%2C+5th+Edition-p-9780470245996> (accessed on 21 June 2019).
38. Taranovich, S. Humidity Sensors and Signal Conditioning Choices DigiKey. Available online: <https://www.digikey.com/en/articles/techzone/2011/oct/humidity-sensors-and-signal-conditioning-choices> (accessed on 20 June 2019).
39. Kaajakari, V. Noise in Micromechanical Systems. Available online: <http://www.kaajakari.net/~ville/research/tutorials/tutorials.shtml> (accessed on 19 June 2019).
40. Buchhold, R. A Study on the microphysical mechanisms of adsorption in polyimide layers for microelectronic applications. *J. Electrochem. Soc.* **2006**. [CrossRef]
41. Godin, M.; Tabard-Cossa, V.; Grütter, P.; Williams, P. Quantitative surface stress measurements using a microcantilever. *Appl. Phys. Lett.* **2001**, *79*, 551–553. [CrossRef]
42. Banerjee, N.; Banerjee, A.; Hasan, N.; Pandey, S.S.; Gogoi, B.P.; Mastrangelo, C.H. A Monolithically integrated multisensor platform. *IEEE Sens. J.* **2016**. [CrossRef]
43. Banerjee, N.; Banerjee, A.; Pandey, S.S.; Gogoi, B.P.; Mastrangelo, C.H. Encroachment and line of sight blocking in micro-cavity sealing. In Proceedings of the 2015 IEEE Sensors, Busa, Korea, 1–4 November 2015. [CrossRef]
44. HD Microsystems, HD—4100 Series Photodefineable Polyimide. Available online: <http://www.hdmicrosystems.com/ec/liquid-polyimides-and-pbo-precursors/products/sub-products/hd-4100-series.html> (accessed on 2 June 2019).

45. Mastrangelo, C.H. Suppression of stiction in MEMS. *MRS Proc.* **1999**. [[CrossRef](#)]
46. Maboudian, R.; Ashurst, W.R.; Carraro, C. Self-assembled monolayers as anti-stiction coatings for MEMS: Characteristics and recent developments. *Sens. Actuators A Phys.* **2000**. [[CrossRef](#)]
47. Banerjee, A.; Pandey, S.S.; Mastrangelo, C.H. MEMS stiction suppression with sacrificial polystyrene nanoparticles. In Proceedings of the IEEE Sensors, Glasgow, Scotland, 29 October–1 November 2017. [[CrossRef](#)]
48. Sensortec, B. BME280—Combined Humidity, Pressure and Temperature Sensor, Datasheet. Available online: [https://www.bosch-sensortec.com/en/bst/products/all\\_products/bme280](https://www.bosch-sensortec.com/en/bst/products/all_products/bme280) (accessed on 29 May 2019).
49. Tang, W.C.; Lim, M.G.; Howe, R.T. Electrostatic comb drive levitation and control method. *J. Microelectromech. Syst.* **1992**. [[CrossRef](#)]
50. Tagne, N.R.S.; Njeugna, E.; Fogue, M.; Drean, J.-Y.; Nzeukou, A.; Fokwa, D. Study of water absorption in raffia vinifera fibres from Bandjoun, Cameroon. *Sci. World J.* **2014**. [[CrossRef](#)]
51. Luna, R.; Millán, C.; Domingo, M.; Santonja, C.; Satorre, M.Á. Experimental study of the frequency factor in the Polanyi–Wigner equation: The case of C<sub>2</sub>H<sub>6</sub>. *Vacuum* **2015**, *122*, 154–160. [[CrossRef](#)]



© 2019 by the authors. Licensee MDPI, Basel, Switzerland. This article is an open access article distributed under the terms and conditions of the Creative Commons Attribution (CC BY) license (<http://creativecommons.org/licenses/by/4.0/>).